Cellulose (2023) 30:6149–6162
https://doi.org/10.1007/s10570-023-05258-w

ORIGINAL RESEARCH

Cellulose solubility in ionic liquids and regeneration in water and hydrogen peroxide solution: a comparative examination of morphology and physicochemical properties

Stacy A. Love · Ethan Magaziner · Diana S. Melissaratos · Sneha Seelam · David Salas-de la Cruz

Received: 21 July 2022 / Accepted: 10 May 2023 / Published online: 20 May 2023

Abstract The main objective of this work is to present a comprehensive analysis of the morphology, topography, and thermal behavior of modified cellulose as a function of solvation temperature, ionic liquid type, and regeneration agent. Avicel microcrystalline cellulose was dissolved at two temperatures (73 °C and 100 °C) in two competing imidazolium-based ionic liquids (1-ethyl-3-methylimidazolium acetate and 1-ethyl-3-methylimidazolium bromide). Aliquots of each solvent-polymer mixture were then washed and regenerated in competing baths (D.I. water and 25% hydrogen peroxide solution). A comparative analysis of the work is that the solvation temperature and ionic liquid counterion (AcO^- and Br^-) had direct relationships to polymer solubility and physicochemical properties of the cellulose samples. Also, treatment of hydrogen peroxide solution as a regenerative agent influenced crystal sizes within the samples. Partial dissolution of cellulose induced by 1-ethyl-3-methylimidazolium bromide influenced the production of unique morphological changes and thermal behaviors relative to microcrystalline cellulose and other cellulose preparations.

Keywords Cellulose I · Cellulose II · Polymorphism · Ionic liquids · Morphology · Hydrogen peroxide

Supplementary Information The online version contains supplementary material available at https://doi.org/10.1007/s10570-023-05258-w.

S. A. Love · S. Seelam · D. Salas-de la Cruz (✉)
The Center for Computational and Integrative Biology, Rutgers University–Camden, 315 Penn Street, Camden, NJ 08102, USA
e-mail: ds1191@camden.rutgers.edu

E. Magaziner · D. S. Melissaratos
Department of Biology, Rutgers University–Camden, 315 Penn Street, Camden, NJ 08102, USA

E. Magaziner · D. Salas-de la Cruz
Department of Chemistry, Rutgers University–Camden, 315 Penn Street, Camden, NJ 08102, USA

Introduction

Facile procedures to modify natural polymers for biomaterials and other technologies are important for the advancement of greater eco-friendly technologies. In fact, there is an emphasis on fine-tuning specific biopolymer properties such as morphology, biocompatibility, and thermal behavior due to a myriad of possible applications. Examples include but are not limited to packing materials (Rhim and Ng 2007), food engineering, e.g., encapsulation and binding agents (Jones and McClements 2010; Khan et al. 2007), and biomaterials such as implants, tissue scaffolds, drug delivery systems, and polymer therapeutics (Hadadi et al. 2018; Metzke and Guan 2008). In general, biopolymers serve as an ideal material that can be widely incorporated in research due to their relatively high abundance from natural resources, low

economical cost, human biocompatibility, and useful physicochemical properties (Metzke and Guan 2008; Song et al. 2018). The global market sales of biomaterials reached nearly $400 billion in the beginning of the twenty-first century and are expected to grow in value (Yin and Luan 2016). Notably, one type of biopolymer, cellulose, remains the most abundant on Earth due to its production in an extensive range of living organisms, e.g., roughly 33% of all plant matter (Wang et al. 2012). Cellulose is a polysaccharide composed of poly-β(1,4)-D-glucose residues and is commonly noted as the structural component found in the plant cell wall (Wang et al. 2012). Cellulose is frequently utilized for scientific inquiry, largely due to its strong inter- and intramolecular forces (Helbert et al. 1998) and useful material properties. Cellulose as a molecule is dimorphic in nature and comes in the forms Iα and Iβ. Cellulose Iα is the dominant allomorph (crystal form) for algae and bacteria, whereas cellulose Iβ is the major component in plant cell walls. The spatial groups and chain packing of the Iα and Iβ phases differ; cellulose Iα has a triclinic unit cell while cellulose Iβ has a monoclinic unit cell made from two parallel chains (Perez and Samain 2010). In particular, Avicel microcrystalline cellulose (MCC) is a popular cellulose preparation to study and is used in a wide range of industry products including cosmetics, plastics, food, and pharmaceuticals (Das et al. 2010). MCC is comprised of cellulose Iβ and can be further modified to a cellulose II structure which is characterized by anti-parallel sheets as opposed to the parallel sheets of cellulose I. Even though cellulose II is infrequently found in nature, it may be produced through a process of dissolution and regeneration or an alkaline treatment known as mercerization (Cheng et al. 2011; Helbert et al. 1998). Due to a chain rearrangement in the conversion of cellulose I to II, it is reported that cellulose II is more thermally stable than its cellulose I counterpart (Ishikawa et al. 1997). Therefore, since cellulose II contains useful properties within the field of biomaterials and other technologies, it is important to study the variations in chemicals and solvation temperatures used for its fabrication.

Choice of solvent is crucial for cellulose regeneration because the transition between crystal forms is influenced by the miscibility of the solvent-polymer matrix. In general, another significant property for proper polymer dissolution is temperature because an increase in kinetic energy of the system allows the solvent molecules to disrupt intermolecular forces more effectively. Most typical organic solvents cannot dissolve cellulose due to the polymer's relatively strong intermolecular forces and tight chain packing formations (Li et al. 2011; Medronho and Lindman 2015; Zhang et al. 2005). Therefore, ionic liquids (IL) may be used to dissolve cellulose into separate, shorter polymer chains without total degradation of the monomer unit. ILs are molten salts comprised of organic cations and either organic or inorganic anions known here as counterions. Cation examples include 1-butyl-3-methylimidazolium ($BMIM^+$), 1-ethyl-3-methylimidazolium ($EMIM^+$), and 1-methyl-3-methylimidazolium ($MMIM^+$), while some of many counterions within ILs are bromide (Br^-), chloride (Cl^-), acetate (AcO^-), and 2,2-Dimethoxypropane (DMP^-) (Cao et al. 2017). Relative to other organic solvents, many ILs have low vapor pressures, wide electrochemical windows, increased thermal stabilities, and moderate ionic conductivities (Johnson 2007). Therefore, ILs possess favorable properties for the dissolution of large, complex organic molecules like cellulose. When introduced to the IL solvent, the hydroxy group of cellulose associates with charged ions of the IL (Mohd et al. 2017). For example, anions like AcO^- are a strong hydrogen bond acceptor, and it is known that strong nucleophilic abilities of a solvent will lead to greater solubility. Additionally, hydrogens at site C2 in an imidazolium cation of an IL can interact with the hydroxy oxygen of cellulose. Upon dissolution, this interaction will assist in the disruption of the polymer's interchain and intrachain hydrogen bonds. (Sun et al. 2014). As a result of such complex and wide-ranging solution capabilities, the IL-cellulose matrix, coupled with appropriate regeneration agents, is seen as a supplementary environment for the formation of varying polymorphism in cellulose. To emphasize, certain RT ILs such as $[MMIM]^+DMP^-$ and $[EMIM]^+DEP^-$ help facilitate a change from crystalline type I to type II through a rearrangement of molecular morphology upon dissolution and later purification in water and ethanol (Zhao et al. 2012). One aspect of this study reports on the solution capabilities of two imidazolium-based ILs where only the counterions are different, i.e., 1-ethyl-3-methylimidazolium acetate, $[EMIM]^+AcO^-$, and 1-ethyl-3-methylimidazolium bromide, $[EMIM]^+Br^-$. Each solvent was chosen for this study due to their different properties where $[EMIM]^+AcO^-$ is liquid at room

temperature and has a relative density of 1.027 g/cm^3 at 25 °C, while [EMIM]$^+$Br$^-$ has a melting point range of 70–73 °C and a relative density of 1.340 g/cm^3 at 25 °C. These specific ILs have been successfully used within the scientific community for the past 10 years. The work reported here elucidates some of the structural changes as a function of IL type that was missing from the literature. By changing the counterion within these imidazolium-based solvents, a more comprehensive study can be examined regarding the nucleophilic capabilities between AcO$^-$ and Br$^-$. After the dissolution process, the IL-polymer mixture is submerged in another solvent; this regeneration phase will simultaneously diffuse IL molecules and regenerate the cellulose polymer (Blessing et al. 2019; Love et al. 2020; Stanton et al. 2017, 2018).

Within this study, MCC is modified into eight different cellulose-samples and properties such as solubility, topography, polymorphism, and thermostability are studied as functions of solvent counterion, solvation temperature, and regeneration agent. Two imidazolium-based ILs, [EMIM]$^+$AcO$^-$ and [EMIM]$^+$Br$^-$, are compared and reported at two temperatures, 73 °C versus 100 °C, which allows for evaluating proper miscibility of the solvent-polymer mixtures. A subsequent regeneration phase was conducted where solvent-polymer aliquots were bathed in competing solutions, D.I. water and 25% hydrogen peroxide. Cellulose characteristics as a function of fabrication parameters are reported within this comparative study. Structural, topographical, thermal, and morphological properties of the modified celluloses were characterized by Fourier Transform Infrared Spectroscopy (FTIR), Scanning Electron Microscopy (SEM), Thermogravimetric Analysis (TGA), and Wide-angle X-ray Scattering (WAXS), respectively. Analysis of this study's data will provide fundamental knowledge to the understanding of a transition between cellulose I, cellulose II, and amorphous cellulose based on fabrication parameters alone.

Materials and methods

Chemicals

Avicel microcrystalline cellulose was purchased from Analtech (CAT-No. P05031). The chemicals, 1-ethyl-3-methylimidazolium acetate ≥ 95.0% (CAS-No. 143314-17-4), 1-ethyl-3-methylimidazolium bromide ≥ 97.0% (CAS-No. 65039-08-9), and ACS reagent-grade (Quality Level 200) hydrogen peroxide solution at 30 wt.% in water with inhibitor (CAS-No. 7722-84-1) were purchased from Sigma Aldrich, USA. The MCC powder and ionic liquids were placed in a vacuum oven set to 30 inHg at 50 °C (24 h) for moisture removal (Liu et al. 2011). Stock hydrogen peroxide solution was stored at 4 °C and diluted to 25 vol.% in D.I. water prior to use.

Fabrication of cellulose-samples

Regenerated cellulose-samples were fabricated using a total mass ratio of 10% Avicel microcrystalline cellulose and 90% solvent (ionic liquid). For a comparative analysis, the solvent was heated in a silica oil bath at either 73 °C or 100 °C, and Avicel microcrystalline cellulose was slowly added for dissolution or partial dissolution. After all cellulose was added, the solution stirred on a hotplate for 24 h. Then, the solvent-cellulose mixture was placed onto glass slides. Cellulose-sample were approximately 1 mm thick with a diameter of 1–1.5 cm, some samples broke during the fabrication process. Photographs of all samples are in the Online Resource (**SI. 1**). Two competing regeneration agents were prepared, D.I. water and 25% hydrogen peroxide solution. The glass slide containing the solution of dissolved cellulose and solvent was placed in a regeneration bath and sealed with Parafilm to prevent evaporation and contamination. The baths were left undisturbed for 48 h at RT. After cellulose regeneration, the samples were removed from the regeneration baths and placed in Petri dishes. This final product was dried in a vacuum oven set to 30 inHg at 50 °C for 24 h. The dried products were then placed in glass vials and sealed in a desiccator set to 15–20 in for long-term storage.

Characterization

Fourier transform infrared spectroscopy

A Bruker's ALPHA-Platinum Attenuated Total Reflectance Fourier Transfer Infrared Spectrometer was used for chemical analysis of the cellulose-samples. A Platinum-Diamond sample module was used and the software, Opus 7.2, generated spectra between 4000–400 cm^{-1} with a resolution of 4 cm^{-1}

per scan. The scanning parameters were set to 128 background scans along with 32 sample scans on six different areas of the samples; the mean result was chosen for final analysis. Data were normalized using min–max normalization for comparative and visualization purposes. Further information regarding the precise wavenumber values of all IR peaks is reported in the Online Resource (**SI. 2–10**).

Scanning electron microscopy

Imaging of the samples' topography was conducted using a JOEL JCM-6000 Scanning Electron Microscope with an accelerating voltage set to 15 kV. A DII-29010SCTR Smart Coater was used to sputter-coat samples for 60 s in a vacuum of 4 Pa. Sample coating consisted of an alloy, Au-Pt, which was done to reduce surface charge and increase conductivity during imaging. Within this study, images at 500 × magnification are reported; other images, 50x, 100x, and 1000x, are in the Online Resource (SI. 11–18).

Thermogravimetric analysis

Thermal behavior is reported using Thermogravimetric Analysis. Samples of 2.5–3 mg were placed in an aluminum pan for data acquisition by a TA Instruments Discovery Series TGA system. Prior to heating, the chamber was purged in nitrogen gas at a rate of 25 mL/min. Sample measurement began at 30 °C. After an isothermal period of 60 s, the temperature was ramped at a rate of 10 °C/min to 600 °C. Subsequent to data acquisition, a step transition analysis was used to calculate the temperature onset (T_o) and temperature end (T_f) of decomposition as well as the percent of total weight loss. The samples' fastest rate of change in weight loss as a function of temperature (ΔT_p) were calculated and reported. Thermograms show negative derivatives for visualization purposes.

X-ray scattering

Morphological studies were conducted using a Xeuss 2.0 Dual Source Environmental X-ray Scattering system at the University of Pennsylvania. Data acquisition was performed under vacuum. A copper x-ray source was used for incident radiation, and a 1 M Pilatus solid-state detector was used for wide-angle scattering (WAXS); $\lambda = 1.54189$ Å. Acquisition of data was performed for samples positioned at random orientation, using full flux collimation with a 1.2 mm × 1.2 mm slit for a 600 s scan-time. Using Foxtrot 3.4.9, isotropic 2-D scattering patterns were converted by azimuthal integration to yield a 1-D profile of intensity (a.u.) versus scattering vector q (nm^{-1}). Bragg's equation was used to calculate values for d-spacing. The plots were then converted to intensity versus $2\theta(^\circ)$ so that the crystal size could be calculated by the Scherrer equation:

$$\tau_{hkl} = \frac{K\lambda}{(FWHM_{hkl})\cos\theta_{hkl}}$$

where τ_{hkl} is the mean size of the crystal; K is the dimensionless shape factor (0.94); λ is the wavelength of the incident x-ray beam (0.154 nm); $FWHM_{hkl}$ represents the full width at half-maximum of the scattering peak in radians, and θ_{hkl} is the Bragg angle. A Peak Deconvolution app manufactured by OriginPro 2021 version 1.8 was used for peak analysis. All peaks were set to positive by creating a lower amplitude bound of zero, and a Gaussian–Lorentzian function was performed for peak-fitting until full convergence was achieved; images of fitted peaks and relative data are reported in the Online Resource (SI. 19–26).

Results and discussion

Cellulose-samples produced for this study are categorized by different IL types used during preparation and are subcategorized by their solvation temperatures and regeneration agents. All sample labels and their fabrication parameters are reported and explained in Table 1. Celluloses within their corresponding sample-sets are referred to as the either the "AcO-set" or the "Br-set" when mentioned throughout this study.

Structural analysis was performed with the aid of Fourier Infrared Spectroscopy (FTIR). The normalized spectra of modified celluloses within the AcO-set (Fig. 1a) and Br-set (Fig. 1b) are compared to one another and to a spectrogram of unaltered MCC (Fig. 1c). Bands which represent cellulose's stretching –OH, stretching and bending –CH, and stretching C–O–C modes are seen in profiles of

Table 1 Cellulose-samples are labelled by their fabrication parameters, i.e., *solvent type-solvation temperature-regeneration agent*

Solvent	Solvation temperature	Regeneration agent	Label
$[EMIM]^+AcO^-$	100 °C	25% H_2O_2	AcO100h
		Water	AcO100w
	73 °C	25% H_2O_2	AcO73h
		Water	AcO73w
$[EMIM]^+Br^-$	100 °C	25% H_2O_2	Br100h
		Water	Br100w
	73 °C	25% H_2O_2	Br73h
		Water	Br73w

Within this report, AcO100h, AcO100w, AcO73h, and AcO73w are labelled as samples within the "AcO-set", while the "Br-set" refers to samples, Br100h, Br100w, Br73h, and Br73w

MCC and all regenerated samples within ranges of 3600–3200 cm^{-1}, 3000–2750 cm^{-1}, 1437–1311 cm^{-1}, 1030–1016 cm^{-1}, respectively. Since regenerated cellulose has the ability to retain moisture, a water peak between 1640–1580 cm^{-1} of various intensities appears in all spectra. When comparing data between IL-sets (AcO-set versus Br-set) spectra of the AcO-set show an overall broader peak at the band representative of the hydroxy group located in the functional group region. This "broadening" of the peak is most pronounced within the AcO100h spectrogram relative to all profiles. When compared to the spectrum of MCC, an analogous functional group region appears within profiles of the Br-set. Proper polymer dissolution is dependent on solvent type and solvation temperature; therefore, it is pertinent to note that greater peak changes are seen within IR spectrograms of the AcO-set relative to of those the Br-set. This could be due to greater modifications to both hydrogen bonding and hydroxymethyl confirmations within this type of regenerated cellulose (Crawford and Ismail 2020).

Variations are also seen within the fingerprint region upon comparing the sample spectra to the MCC spectrum. As expected, the main C–O–C band at ≈ 1030 cm^{-1} appears in the spectra of both sample-sets and MCC. However, a side peak at ≈ 1106 cm^{-1} disappears within plots of the AcO-set, thus, showing a discrepancy in spectra between sample-sets. It is noted that only a shoulder and not a distinct peak at this location appears for one of

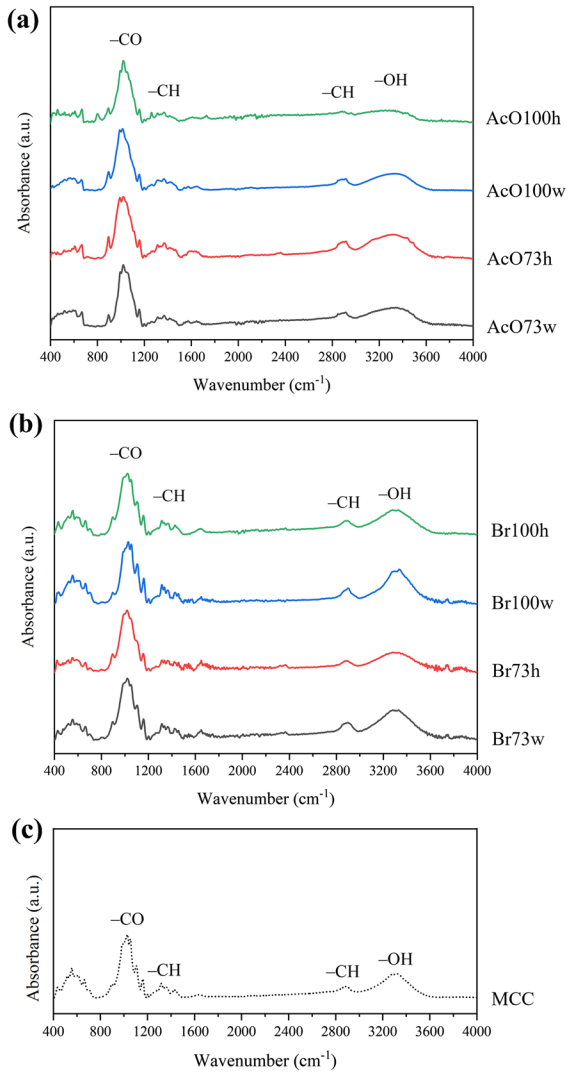

Fig. 1 Normalized FTIR data of cellulose-samples fabricated by the solvents, $[EMIM]^+AcO^-$ (**a**) and $[EMIM]^+Br^-$ (**b**), along with a spectrum of unmodified MCC (**c**). Sample spectrograms are differentiated based on sample type which are listed on the legends. The following prominent IR absorbance bands for cellulose are labelled as stretching –OH (3600–3200 cm^{-1}), stretching –CH (3000–2750 cm^{-1}), absorbed water (1640–1580 cm^{-1}), bending –CH (1437–1311 cm^{-1}), and stretching C–O–C (1030–1016 cm^{-1}). Asterisks denote specific changes in peak appearance and/or intensity

the Br-set's spectra (Br73h) although most of the Br-set's IR spectra is analogous to that of MCC. A second distinct side peak at ≈ 897 cm^{-1} is located on the opposite side of the C–O–C peak in all spectrograms. However, when compared to MCC, this peak only grows in intensity within spectra of the

AcO-set. Furthermore, a deformation of peak shape around the 1428 cm^{-1} region is seen within AcO-set spectrograms relative to the MCC spectrum, and a shift in wavenumber from 1428 cm^{-1} (MCC) to 1420–1414 cm^{-1} (AcO-set) is present. Changes in peak presence/disappearance, intensity, shape, and shifting within the aforementioned fingerprint regions of the AcO-set occur due to morphological modifications during sample fabrication, i.e., a change in crystalline structure when cellulose I transitions to either cellulose II or amorphous cellulose (Astruc et al. 2017; Kavkler et al. 2011). Therefore, the spectra of samples within the AcO-set are representative of cellulose II or a cellulose III type (amorphous cellulose), whereas the spectra of the Br-set retain a profile closer to that of unaltered MCC, i.e., cellulose I. This could be due to fewer interactions between cellulose's intermolecular forces and the counterion Br^- relative to AcO^- during sample dissolution and regeneration. Further information regarding the precise wavenumber values of all IR peaks is reported in the Online Resource (SI. 18–26).

Scanning Electron Microscopy (SEM) was used to report and compare the topographical differences of cellulose-samples within the AcO-set (Fig. 2a) and Br-set (Fig. 2b) to the surface structure of MCC (Fig. 2c); figures show images at 500× magnification. SEM Images of the AcO-set show a mostly smooth topography except for AcO73h where small, irregularly shaped nodules cover its entire surface in a layered formation. Furthermore, when comparing sample topography of the AcO-set as a function of solvation temperature, fracturing of the surface is reported when solvation temperature was increased during fabrication. Nevertheless, images of the AcO-set appear to have a greater homogenous exterior than those of the Br-set.

As expected, images of MCC show that cellulose fibers are distributed in a random order and microcrystalline regions appear with some amorphous structures (Fig. 2c). With this is mind and upon consideration of the AcO-set, images of the Br-set show a partially dissolved fibrillar composition of cellulose. These structures are randomly orientated but differ in their shape and size relative to MCC. Smoother regions infer a greater change to the topography upon fabrication, and it is clear from the images that a total reconstruction of the surface structure occurred for cellulose when dissolved in $[EMIM]^+AcO^-$ and not

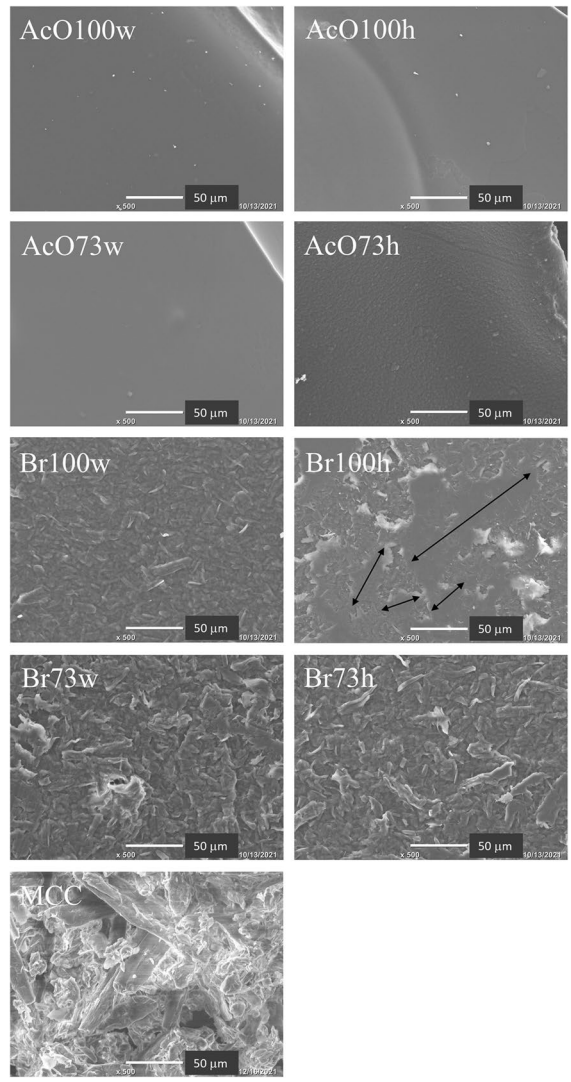

Fig. 2 500× magnified SEM image (bar = 50 µm) of cellulose-samples fabricated by the solvents, $[EMIM]^+AcO^-$ and $[EMIM]^+Br.^-$, and unmodified MCC. All sample images pertaining to the AcO-set show homogenous, smooth topography. Images of the Br-set show fractured cellulose fibers. Arrows depict regions of smooth topography (Br100h)

$[EMIM]^+Br^-$. Additionally, one noticeable difference in Fig. 2b is that Br100h has multiple large aggregates of smooth "zones" similar to the entire surface topography of samples within the AcO-set. In other words, randomized and localized smooth regions with irregular dimensions may be seen in the image of Br100h. Though the image of Br100w shows more topographical changes than those of Br73w and Br73h, it does not show localized smoothness like that of Br100h or

full topographical homogeneity of samples within the AcO-set.

Recalling the solvation phase during the fabrication of cellulose preparations, it is pertinent to note that the $[EMIM]^+Br^-$/polymer solution was considerably more viscous than the $[EMIM]^+AcO^-$/polymer solution. It is known that viscosity is directly proportional to the hydrodynamic volume of a polymer within its solution and therefore, a more viscous solution will increase microphase separation within the system. From this, it is deduced that more microphase separation occurred within the $[EMIM]^+Br^-$/polymer solution relative to the $[EMIM]^+AcO^-$/polymer solution. However, increasing the temperature of a solution also increases miscibility of the polymer and solvent; this is partly due to the fact that entropy increases with an increase in temperature and must overcome the enthalpy of the system for proper miscibility. Since increasing the solvation temperature increases miscibility, samples dissolved at a higher temperature had more structural changes. Case in point, SEM images of Br100w and Br100h show a greater topographical change than those of Br73w and Br73h. In addition, previous studies on other biopolymers, such as blends of cellulose-silk films, have reported reduced surface topography homogeneity in products dissolved in 1-butyl-3-methyl imidazolium bromide (Stanton et al. 2018), further corroborating the proposition that $[EMIM]^+Br^-$ partially dissolves cellulose and indicating inferior miscibility rather than molecular weight degradation. During coagulation, the cellulose structure is protected by water molecules through hydrogen bonding, which prevents potential degradation from the ionic liquids. To induce molecular weight degradation, the solution must be subjected to a metal catalyst in conjunction with a high concentration of hydrogen peroxide, which is a standard method for producing white paper from cotton through hydrolysis and bleaching. However, greater reformation of the topography still occurred as a function of an increase in dissolution temperature and subsequent hydrogen peroxide treatment. This combined effect enabled hydrogen peroxide molecules to compete in the interaction of solvent ions and hydroxy groups of the cellulose. These events ultimately changed the cellulose topography and helps to explain the apparent variation in topographical complexity such as smooth areas versus irregular regions.

Thermal behaviors of MCC and its modified celluloses are shown in Fig. 3a–d. Refer to Table 2 for data pertaining to the temperature onset (T_o) and end (T_f) of degradation, final weight loss percent, and maximum change of rate in weight loss percent as a function of temperature (ΔT_p). When multimodality appears within the derivative's plot, the maxima at different temperatures are labelled separately as ΔT_{p1} and ΔT_{p2}. Thermal characteristics of the cellulose-samples vary depending on all three fabrication parameters: IL counterion, temperature during polymer dissolution, and the chemical agent used for polymer regeneration. It is proposed that solvent type, especially the counterions of $[EMIM]^+AcO^-$ and $[EMIM]^+Br^-$, has a significant effect on the thermal stability of regenerated cellulose. This is partially due to the solubility capabilities of the competing solvents where the counterion of $[EMIM]^+AcO^-$ acts as a better nucleophile than that of $[EMIM]^+Br^-$. The range of T_o for samples within the AcO-set is depressed relative to those in the Br-set, where T_o values are reported to be 195.68–255.19 °C and 253.57–283.47 °C for the AcO- and Br-sets, respectively. There is one exception to this statement in which two values are significantly similar, e.g., T_o values for AcO100h (255.19 °C) and Br100h (253.57 °C). Therefore, when the dissolution temperature is higher and a subsequent treatment of hydrogen peroxide is used for coagulation, similarities in the onset temperature of thermal degradation are reported. Relative to MCC where the T_o value is 319.66 °C, cellulose-samples within both sets have lower onset values. However, changes in degradation rate and weight loss percent indicate a more thermally stable material than MCC. This makes sense considering the change in cellulose polymorphism, i.e., cellulose Iβ to II or III, upon dissolution and regeneration of the samples.

MCC has a higher T_f value than both IL-sets except for AcO100h, and a trend of elevated values is calculated for all celluloses regenerated in hydrogen peroxide solution relative to water. However, this trend does not follow for total weight loss percent. For example, MCC has a total loss of 96.01% while samples of the AcO-set range between 86.95–82.75% where percent loss is greater for samples treated with water relative to hydrogen peroxide solution. Upon exclusion of Br100w with a mass loss at 88.65%, values for the Br-set are between 71.94–74.23%.

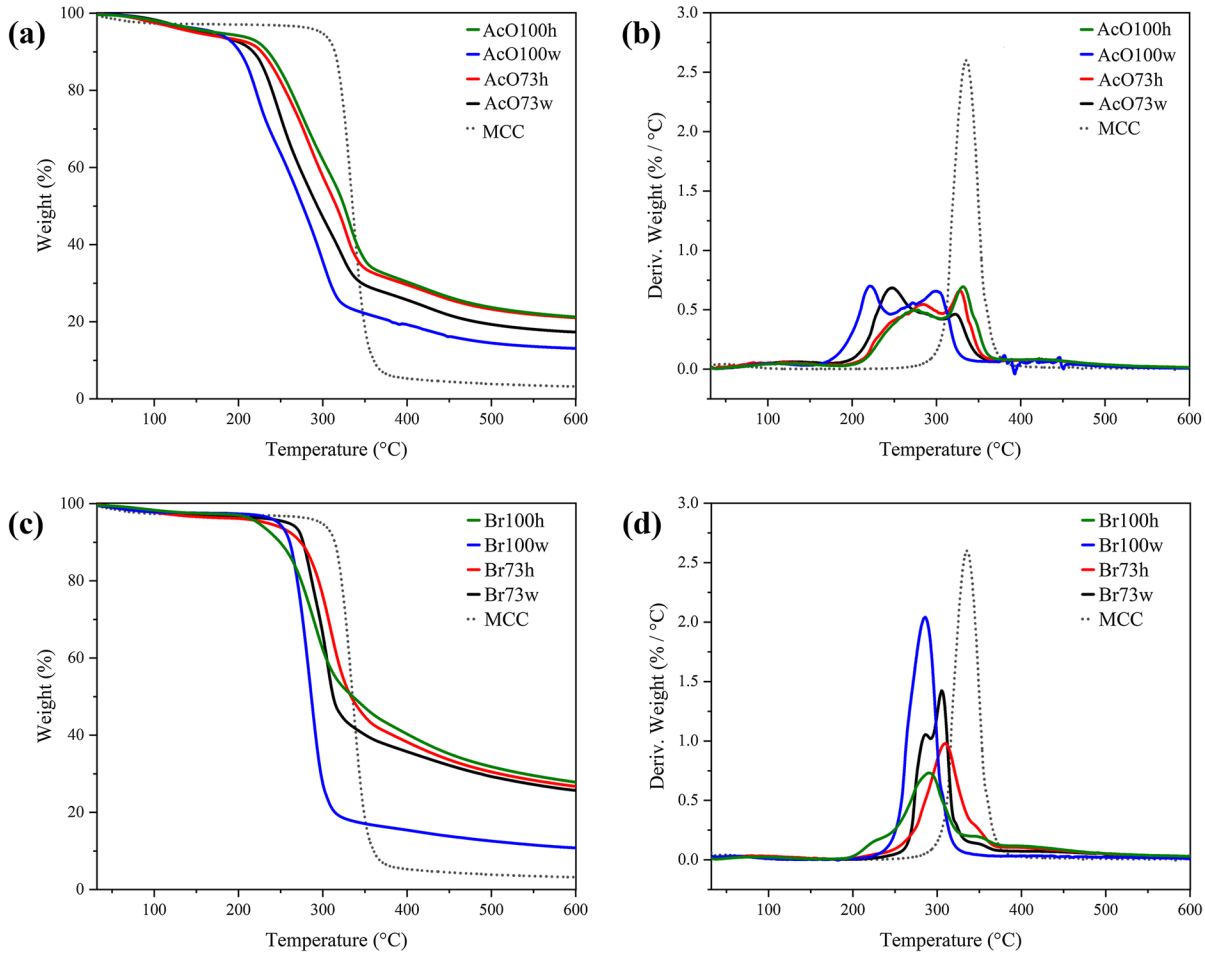

Fig. 3 Thermograms for MCC (dotted lines) and modified celluloses (solid lines). Plots show weight loss percent as a function of increasing temperature (**a**) and its derivative (**b**) for samples within the AcO-set. Likewise, **c**, **d** show the same thermogram types for data of the Br-set. Thermogram derivatives are shown as unimodal for MCC, multimodal for modified celluloses within the AcO-set and a mixture of unimodal and multimodal for samples within the Br-set

Table 2 TGA data for MCC and modified cellulose-samples

Sample	T_o (°C)	T_f (°C)	Weight (%)	ΔT_{p1}	Temp. (°C)	ΔT_{p2}	Temp. (°C)
MCC	319.66	352.85	96.01	2.60	335.18	–	–
AcO100h	255.19	361.88	78.69	0.43	302.7	0.69	331.94
AcO100w	195.68	318.75	86.95	0.70	222.42	0.66	299.81
AcO73h	243.81	357.41	79.18	0.55	283.86	0.66	326.84
AcO73w	215.42	327.32	82.75	0.68	247.91	0.46	322.21
Br100h	253.57	334.18	71.94	0.72	288.58	–	–
Br100w	264.86	303.34	88.65	0.71	285.79	–	–
Br73h	283.47	342.61	73.13	0.98	308.28	–	–
Br73w	280.67	322.81	74.23	1.05	280.67	1.42	322.81

Values are reported for temperature onset of degradation (T_o), temperature end of degradation (T_f), final weight loss percent, and the maximum change of rate in weight loss as a function of temperature (ΔT_p). When multimodality is calculated, the maxima at different temperatures are labelled separately (ΔT_{p1} and ΔT_{p2})

Therefore, most celluloses within the Br-set have greater thermal stability than all other samples. Notably, the Br-set's hydrogen peroxide-treated samples are the most thermally stable, i.e., Br100h and Br73h at 71.94% and 73.13%, respectively.

Another obvious difference between the thermograms of the two IL-sets relative to MCC is their plot derivatives ($\Delta T_{p1,p2}$). MCC's rate of degradation is quick with one step-transition, but two major step-transitions occur within plots of the AcO-set resulting in multimodal derivatives. This means that multiple regions of sample degradation occurred at different temperatures. Multimodality in thermograms is typical when areas of crystallinity or semi-crystallinity degrade at slower rates than amorphous structures (Hadadi et al. 2018). Furthermore, samples such as AcO100w, AcO73w, AcO73h, and AcO100h have maxima values $\Delta T_{p1} = 0.70$, 0.68, 0.55, and 0.43 respectively. Here, water-treatments of cellulose act to increase degradation rates at lower temperatures. Celluloses treated in hydrogen peroxide solution have peak shapes very similar to one another, and their rates of degradation are slower at ΔT_{p1} and faster at ΔT_{p2}. This proves that the thermal degradation rate of cellulose within the AcO-set changes as a function of regeneration agent (water versus 25% hydrogen peroxide).

Conversely, fewer step transitions per sample were calculated for celluloses within the Br-set. In fact, this thermogram shows unimodal derivatives for most of the samples, confirming one step transition of degradation. The rate of degradation of Br100w is analogous to that of MCC, while degradation rates of Br100h and Br73h are slower than their water-regenerated counterparts. This may be due to the morphology or crystallinity of the hydrogen peroxide-treated celluloses. It has been reported that increasing percentages of hydrogen peroxide solution increases cellulose crystal size upon fabrication and that larger crystals embedded within the cellulose matrix will degrade at slower rates than smaller ones (Hadadi et al. 2018; Love et al. 2020). Interestingly, bimodality is seen in the thermal derivative of Br73w where $\Delta T_{p1} = 1.05$ at 280.67 °C and $\Delta T_{p2} = 1.42$ at 322.81 °C. An explanation for this is that when a lower solvation temperature is coupled with a subsequent water bath treatment, the resulting product contains both amorphous and slight semi-crystalline structures. The purely amorphous forms degrade slower and at lower temperatures (ΔT_{p1}) than its semi-crystalline regions (ΔT_{p2}). Derivative multimodality versus unimodality is further proof that $[EMIM]^+AcO^-$ as a solvent changes the morphologies of fabricated samples more significantly when compared to $[EMIM]^+Br^-$. However, thermograms of celluloses made from $[EMIM]^+Br^-$ show greater thermal stability regarding the samples' total weight loss percent, notably for those produced from a treatment of hydrogen peroxide solution.

Investigation into the crystalline structure of cellulose preparations was performed via Wide-angle X-ray Scattering (WAXS). Refer to Fig. 4a–i for WAXS 1-D profiles of the AcO-set, Br-set, and MCC, respectively. All x-ray scattering data are reported in Table 3 and include reflections in 2θ and scattering vector q with their corresponding values for the peaks' full width at half-maximum $FWHM_{hkl}$, crystal size τ_{hkl}, and interplanar spacing d. The ranges of d-spacing values for all celluloses are calculated to be 0.72–0.70 nm, 0.61–0.59 nm, 0.55–0.54 nm, 0.44–0.43 nm, 0.40–0.39 nm, and 0.26–0.25 nm for reflections at ~ 12°, 14°, 16°, 20°, 22°, and 35° respectively. MCC is known to consist of a cellulose Iβ crystal structure, so all crystal size values of preparations were comparatively analyzed to help determine different states of periodic order within their crystalline morphologies.

Cellulose profiles of the AcO-set show either cellulose II reflections or an amorphous halo. Typical cellulose II profiles show a reflection at ~ 12° and a doublet at ~ 20° and 22°, while amorphous cellulose has a single broad halo located at ~ 20°. In particular, the profile of AcO73w contains a broad halo at 20.22°. The value calculated as the "crystal size" at this site is relatively small, $\tau_{hkl} = 2.92$ nm, and the peak shape is too broad to be considered semi-crystalline. As a result, this halo is indicative of a structure that is amorphous, and the calculated τ_{hkl} serves only as a comparative value to the crystal size of actual semi-crystalline samples. Two overlapping yet discernible scattering peaks at 19.96 and 21.54° appear in the profile of AcO100w, and when considering water-treated samples, an increase in solvation temperature had a significant effect on the morphology of the regenerated celluloses. The peak at 21.54° represents a change in crystal size because its presence decreases the full-width at half value of the peak at 19.96°. In other words, peak sharpness is inversely

Table 3 Wide-angle x-ray scattering data for unaltered MCC and cellulose-samples

Sample	Miller Index	q (nm^{-1})	d (nm)	2θ (°)	$FWHM_{hkl}$	τ_{hkl} (nm)
MCC	1–10	10.61	0.59	14.94	–	–
	110	11.57	0.54	16.30	–	–
	102, 012	14.50	0.43	20.46	1.26	6.46
	200	16.07	0.39	22.72	1.17	6.93
	004	24.53	0.26	34.99	–	–
AcO100h	1–10	8.76	0.72	12.32	–	–
	110	14.37	0.44	20.28	0.41	19.71
	020	15.87	0.40	22.43	0.40	20.51
	004	24.84	0.25	35.45	–	–
AcO100w	1–10	8.80	0.71	12.38	–	–
	110	14.14	0.44	19.96	1.91	4.27
	020	15.25	0.41	21.54	0.95	8.55
	004	24.49	0.26	34.93	–	–
AcO73h	1–10	8.78	0.72	12.35	–	–
	110	14.41	0.44	20.34	0.84	9.72
	020	15.91	0.39	22.49	0.70	11.63
	004	24.80	0.25	35.38	–	–
AcO73w	010	9.00	0.70	12.67	–	–
	100,1–10	14.32	0.44	20.22	2.80	2.92
	004	24.66	0.25	35.19	–	–
Br100h	1–10	10.49	0.60	14.77	–	–
	110	11.42	0.55	16.10	–	–
	102, 012	14.55	0.43	20.55	1.27	6.43
	200	16.05	0.39	22.68	1.58	5.14
	004	24.57	0.26	35.05	–	–
Br100w	1–10	10.58	0.59	14.91	–	–
	110	11.64	0.54	16.40	–	–
	102, 012	14.60	0.43	20.61	1.28	6.39
	200	16.14	0.39	22.81	1.56	5.20
	004	24.66	0.25	35.18	–	–
Br73h	1–10	10.30	0.61	14.51	–	–
	110	11.74	0.54	16.55	–	–
	102, 012	14.55	0.43	20.55	1.05	7.81
	200	16.05	0.39	22.68	1.40	5.79
	004	24.62	0.26	35.12	–	–
Br73w	1–10	10.45	0.60	14.72	–	–
	110	11.51	0.55	16.22	–	–
	102, 012	14.60	0.43	20.61	1.47	5.57
	200	16.09	0.39	22.75	1.62	5.02
	004	24.39	0.26	34.78	–	–

Prominent reflections with their respective miller indices are reported along with calculated values for their scattering vector (q), lattice interplanar-spacing (d), and 2θ conversion from q. The full width at half-maximum ($FWHM_{hkl}$) and crystal size (τ_{hkl}) are noted at ~ 20 and 22°, where typical x-ray crystalline reflections are reported for cellulose

related to crystal size and thus, the τ_{hkl} value at the first peak is larger for AcO100w ($\tau_{hkl} = 4.27$ nm) than the broad halo of AcO73w ($\tau_{hkl} = 2.92$ nm). Therefore, cellulose crystal size begins to increase for the AcO-set as a function of solvation temperature. More substantial peak distinction and sharpness appears in the profiles of samples that were treated in 25% hydrogen peroxide solution. Reflections at ~ 20° and 22° within profiles of AcO73h and AcO100h are considered doublets, and when compared to halos,

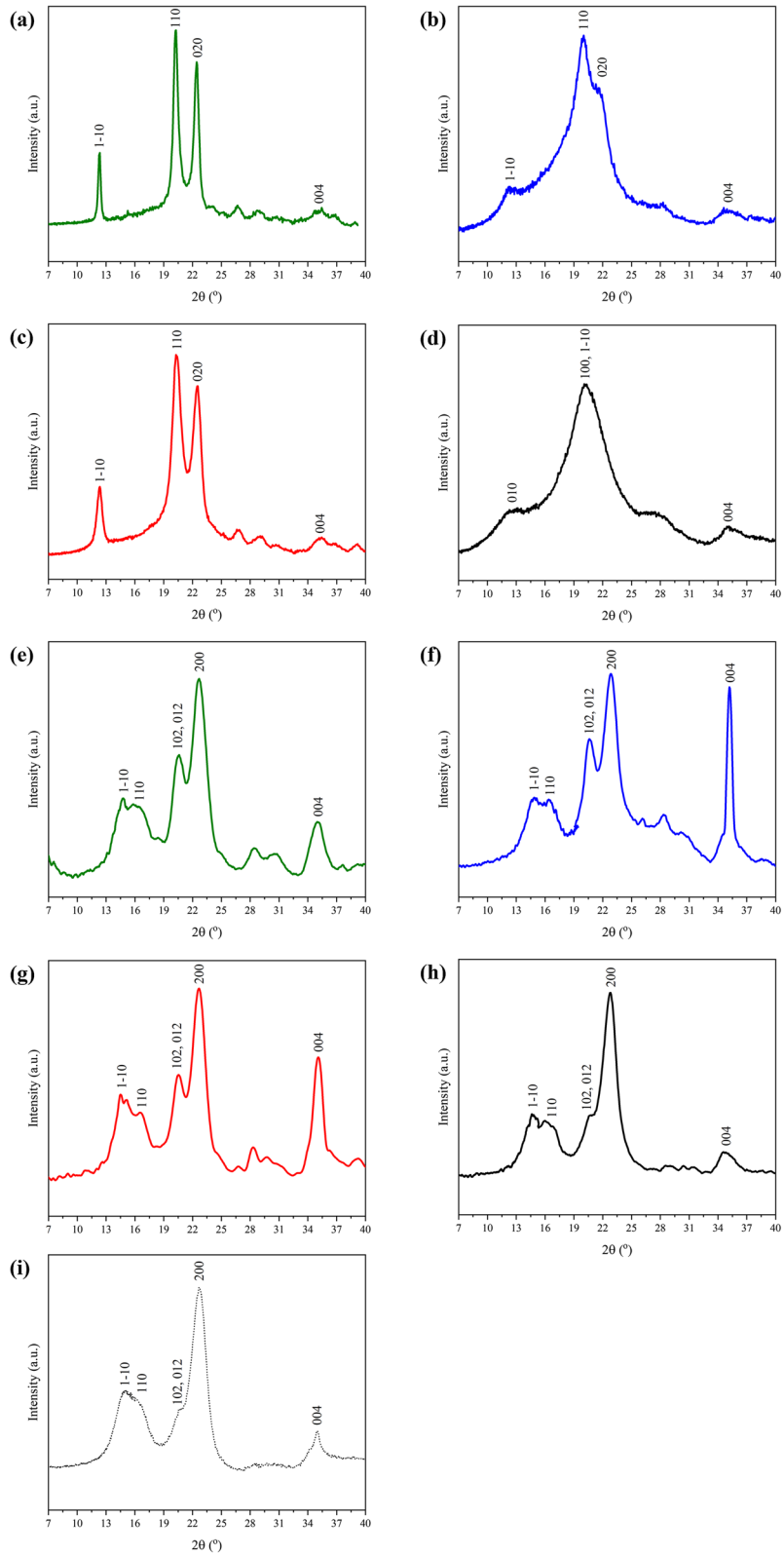

Fig. 4 Wide-angle x-ray scattering 1-D plots of regenerated celluloses, AcO100h (**a**), AcO100w (**b**), AcO73h (**c**), AcO73w (**d**), Br100h (**e**), Br100w (**f**), Br73h (**g**), Br73w (**h**), along with a scattering plot of unmodified MCC (**i**). Prominent Miller indices for cellulose II (**a–c**), amorphous cellulose III_{II} (**d**), and cellulose Iβ (**e–i**) are reported (French 2014)

doublets represent higher crystallinity. In fact, the double peak's crystal sizes within this work were calculated to have a dramatic increase in value relative to the MCC data. When the fabrication parameters for modified cellulose include a high solvation temperature of $[EMIM]^+AcO^-$ and subsequent regeneration in hydrogen peroxide solution, crystal size values at ~ 20° and 22° reflections increase twofold. Interestingly, the calculated τ_{hkl} values at the ~ 22° reflection is larger for AcO100w (8.55 nm) than for MCC (6.93 nm).

When comparing sample data between sample-sets, it is obvious that sample crystallinity is affected by its solvent type. This is seen by changes in peak shifts and shapes within the 1-D profiles. In fact, WAXS plots of the Br-set's samples show reflections indicative of a modified cellulose Iβ form structure. Here, some profiles clearly resemble the cellulose I type of MCC while others show a higher intensity at reflection ~ 20° relative to 22°—which is not suggestive of a typical cellulose I polymorph. The interpretation of this is that there is a modified polymorphic phase within the samples produced by $[EMIM]^+Br^-$. In other words, the crystal form is definitely not cellulose II or III, but also not representative of a perfect cellulose I type. Crystal size values for these samples range between 5.57–7.81 nm for reflection ~ 20° and 5.02–5.79 nm at reflection ~ 22°. These values are close in size to MCC where $\tau = 6.46$ and 6.93 nm for reflections 20.46° and 22.72°, respectively. When considering values at ~ 20° reflection, celluloses regenerated in hydrogen peroxide solution produced slightly larger crystals than their water-regenerated counterparts. However, no significant difference is calculated for crystal size at the ~ 22° reflection site. Refer to Table 3 for precise values.

It is equally important to note that scattering at ~ 35° (reported as Miller index 004) changes as a result of multiple yet subtle fabrication parameters. For example, a reflection at this site shows as a typical representation of cellulose II for all AcO-set samples but is irregular when compared to cellulose I in all profiles of the Br-set with exception to Br73w (Fig. 4h). It is inferred that variations of appearance and intensity at this location represent a change in typical cellulose morphology as a function of solvation type minus the outlier. Curiously, there is a noticeable boost in peak intensity at this site within the profiles of Br100w and Br73h relative to all other cellulose profiles, including that of MCC.

Through analysis of x-ray data, the AcO^- counterion once again proved to be a better nucleating agent than Br^- because samples within the former set show evidence of a clear and distinct polymorphic change. A transition from cellulose I to cellulose II occurred for samples regenerated in hydrogen peroxide baths and amorphous cellulose was produced when samples were regenerated in water. This observation is obvious when considering the 1-D scattering profiles of the cellulose-samples, i.e., shape and intensity of reflections. However, the scattering profiles of the Br-set imply a morphological change where MCC was only partially dissolved upon fabrication. Thus, partially dissolving MCC created cellulose preparations of a modified polymorphic cellulose Iβ formation.

Conclusion

The properties of two sample-sets were characterized as functions of their fabrication parameters, i.e., solvation temperature, solvent counterion, and regeneration identity. Two solvents were compared within this report, $[EMIM]^+AcO^-$ and $[EMIM]^+Br^-$, at two different temperatures, 73 °C and 100 °C. After 24 h of agitated dissolution, aliquots of the solvent-polymer solution were bathed in different regeneration agents, water and 25% hydrogen peroxide solution. Analysis of IR spectroscopy confirmed proper regeneration of the polymer because spectra are analogous to cellulose's main functional groups. In particular, the spectra of samples within the AcO-set resemble a spectrum of cellulose II, whereas the spectra of the Br-set retain an identity closer to that of cellulose I. SEM images depict variations in the topographical complexity of the samples' surface as a function of IL type. Here, dissolution in $[EMIM]^+AcO^-$ produced celluloses with greater changes to its composition than $[EMIM]^+Br^-$, i.e., smooth regions versus fractured surface fibrils. Furthermore, fabrication parameters like solvation temperature and hydrogen peroxide solution played a major role in facilitating topographical changes of the samples. Multiple step-transitions were calculated from the thermal data of the AcO-set while a single step-transition was calculated for a majority of samples within the Br-set. Greater thermal stability with less overall weight loss

is calculated for the Br-set relative to the AcO-set and MCC. WAXS profiles of the AcO-set are representative of cellulose II or amorphous cellulose while those of the Br-set are indicative of a modified cellulose Iβ structure. Overall analysis is that $[EMIM]^+AcO^-$ is an acceptable solvent choice for cellulose when the desired product is either an amorphous cellulose or a cellulose II polymorph through using regenerative baths of water or hydrogen peroxide solution, respectively. Relative to $[EMIM]^+AcO^-$, $[EMIM]^+Br^-$ is a poor solvent for cellulose as it only partially dissolved MCC. However, the modified crystal type formed from using this IL is useful if a regenerated cellulose needs to maintain a crystal formation closer to that of cellulose I while maintaining thermal stability at temperatures typically deleterious to native cellulose.

Acknowledgments A special thank you for the acquisition of x-ray data by *Abneris Morales*, Ph.D. student of The Center for Computational and Integrative Biology at Rutgers University–Camden and for technical support and training on the DEXS system by *Dr. Paul Heiney*, emeritus professor for the Department of Physics and Astronomy at the University of Pennsylvania and supervisor/coordinator for the DEXS facility. Salas-de la Cruz summer financial support was provided by NSF-CMMI (2037097) and NSF-DMR (2104376).

Author contributions Conceptualization: SAL and DS-de laC; Methodology: DS-de laC and SAL; Formal analysis and investigation: SAL, EM, DSM, and SS; Writing—original draft preparation: SAL, EM, DSM, and SS; Writing—review and editing: SAL and DS-de laC; Funding acquisition: DS-de laC; Resources: DS-de laC; Supervision: DS-de laC and SAL.

Funding The authors are grateful for financial support from NSF-DMR-RUI 1809354 and NSF-CMMI 2037097, Rutgers-Camden Arts and Sciences Start-up Package, State of NJ ELF Grant and The Center for Computational and Integrative Biology TA Funds. The DEXS System is supported by NSF-MRSEC 17-20530, NSF-MRI 17-25969, ARO DURIP W911NF-17-1-02822, and the University of Pennsylvania.

Availability of data and materials Supplementary information to this work is available as an online resource.

Declarations

Conflict of interest The authors have no relevant financial or non-financial interests to disclose.

Ethics approval and consent to participate The authors declare no sensitive or personal information is reported within this work.

Consent for publication The authors consent to the publication of this work.

References

Astruc J, Nagalakshmaiah M, Laroche G, Grandbois M, Elkoun S, Robert M (2017) Isolation of cellulose-II nanospheres from flax stems and their physical and morphological properties. Carbohydr Polym 178:352–359

Blessing B, Trout C, Morales A, Rybacki K, Love SA, Lamoureux G, Salas-de la Cruz D (2019) Morphology and ionic conductivity relationship in silk/cellulose biocomposites. Polym Int 68(9):1580–1590

Cao Y, Zhang R, Cheng T, Guo J, Xian M, Liu H (2017) Imidazolium-based ionic liquids for cellulose pretreatment: recent progresses and future perspectives. Appl Microbiol Biotechnol 101(2):521–532

Cheng G, Varanasi P, Li C, Liu H, Melnichenko YB, Simmons BA, Singh S (2011) Transition of cellulose crystalline structure and surface morphology of biomass as a function of ionic liquid pretreatment and its relation to enzymatic hydrolysis. Biomacromol 12(4):933–941

Crawford B, Ismail AE (2020) Insight into cellulose dissolution with the tetrabutylphosphonium chloride–water mixture using molecular dynamics simulations. Polymers 12(3):627

Das K, Ray D, Bandyopadhyay NR, Sengupta S (2010) Study of the properties of microcrystalline cellulose particles from different renewable resources by XRD, FTIR, nanoindentation, TGA and SEM. J Polym Environ 18:355–363

French AD (2014) Idealized powder diffraction patterns for cellulose polymorphs. Cellulose 21(2):885–896

Hadadi A, Whittaker JW, Verrill DE, Hu X, Larini L, Salas-De La Cruz D (2018) A hierarchical model to understand the processing of polysaccharides/protein-based films in ionic liquids. Biomacromol 19(10):3970–3982

Helbert W, Nishiyama Y, Okano T, Sugiyama J (1998) Molecular imaging of halocynthia papillosa cellulose. J Struct Biol 124(1):42–50

Ishikawa A, Okano T, Sugiyama J (1997) Fine structure and tensile properties of ramie fibres in the crystalline form of cellulose I, II IIII and IVI. Polymer 38(2):463–468

Johnson KE (2007) What's an ionic liquid? Electrochem Soc Interface 16(1):38

Jones OG, McClements DJ (2010) Functional biopolymer particles: design, fabrication, and applications. Compr Rev Food Sci Food Saf 9(4):374–397

Kavkler K, Gunde-Cimerman N, Zalar P, Demšar A (2011) FTIR spectroscopy of biodegraded historical textiles. Polym Degrad Stab 96(4):574–580

Khan T, Park JK, Kwon JH (2007) Functional biopolymers produced by biochemical technology considering applications in food engineering. Korean J Chem Eng 24:816–826

Li Y, Lin M, Davenport JW (2011) Ab initio studies of cellulose I: crystal structure, intermolecular forces, and interactions with water. J Phys Chem C 115(23):11533–11539

Liu Z, Wang H, Li Z, Lu X, Zhang X, Zhang S, Zhou K (2011) Characterization of the regenerated cellulose films in ionic liquids and rheological properties of the solutions. Mater Chem Phys 128(1–2):220–227

Love SA, Popov E, Rybacki K, Hu X, Salas-de la Cruz D (2020) Facile treatment to fine-tune cellulose crystals in cellulose-silk biocomposites through hydrogen peroxide. Int J Biol Macromol 147:569–575

Medronho B, Lindman B (2015) Brief overview on cellulose dissolution/regeneration interactions and mechanisms. Adv Colloids Interface Sci 222:502–508

Metzke M, Guan Z (2008) Structure-property studies on carbohydrate-derived polymers for use as protein-resistant biomaterials. Biomacromol 9(1):208–215

Mohd N, Draman SFS, Salleh MSN, Yusof NB (2017) Dissolution of cellulose in ionic liquid: a review. In: AIP conference proceedings (Vol. 1809, No. 1, p. 020035). AIP Publishing LLC

Perez S, Samain D (2010) Structure and engineering of celluloses. Adv Carbohydr Chem Biochem 64:25–116

Rhim JW, Ng PK (2007) Natural biopolymer-based nanocomposite films for packaging applications. Crit Rev Food Sci Nutr 47(4):411–433

Song R, Murphy M, Li C, Ting K, Soo C, Zheng Z (2018) Current development of biodegradable polymeric materials for biomedical applications. Drug Des Dev Ther 12:3117–3145

Stanton J, Xue Y, Waters JC, Lewis A, Cowan D, Hu X, la Cruz DSD (2017) Structure–property relationships of blended polysaccharide and protein biomaterials in ionic liquid. Cellulose 24:1775–1789

Stanton J, Xue Y, Pandher P, Malek L, Brown T, Hu X, Salas-de la Cruz D (2018) Impact of ionic liquid type on the structure, morphology and properties of silk-cellulose biocomposite materials. Int J Biol Macromol 108:333–341

Sun X, Tian Q, Xue Z, Zhang Y, Mu T (2014) The dissolution behaviour of chitosan in acetate-based ionic liquids and their interactions: From experimental evidence to density functional theory analysis. RSC Adv 4(57):30282–30291

Wang H, Gurau G, Rogers RD (2012) Ionic liquid processing of cellulose. Chem Soc Rev 41(4):1519–1537

Yin J, Luan S (2016) Opportunities and challenges for the development of polymer-based biomaterials and medical devices. Regen Biomater 3(2):129–135

Zhang H, Wu J, Zhang J, He J (2005) 1-Allyl-3-methylimidazolium chloride room temperature ionic liquid: a new and powerful nonderivatizing solvent for cellulose. Macromolecules 38(20):8272–8277

Zhao D, Li H, Zhang J, Fu L, Liu M, Fu J, Ren P (2012) Dissolution of cellulose in phosphate-based ionic liquids. Carbohydr Polym 87(2):1490–1494